fractal and fractional

MDPI

Article

Investigation of the Relationship between the 2D and 3D Box-Counting Fractal Properties and Power Law Fractal Properties of Aggregates

Rui Wang *, Abhinandan Kumar Singh, Subash Reddy Kolan and Evangelos Tsotsas

Thermal Process Engineering, Otto von Guericke University, 39106 Magdeburg, Germany
* Correspondence: rui.wang@ovgu.de

Abstract: The fractal dimension D_f has been widely used to describe the structural and morphological characteristics of aggregates. Box-counting (BC) and power law (PL) are the most common methods to calculate the fractal dimension of aggregates. However, the prefactor k, as another important fractal property, has received less attention. Furthermore, there is no relevant research about the BC prefactor (k_{BC}). This work applied a tunable aggregation model to generate a series of three-dimensional aggregates with different input parameters (power law fractal properties: $D_{f,PL}$ and k_{PL}, and the number of primary particles N_P). Then, a projection method is applied to obtain the 2D information of the generated aggregates. The fractal properties (k_{BC} and $D_{f,BC}$) of the generated aggregates are estimated by both, for 2D and 3D BC methods. Next, the relationships between the box-counting fractal properties and power law fractal properties are investigated. Notably, 2D information is easier achieved than 3D data in real processes, especially for aggregates made of nanoparticles. Therefore, correlations between 3D BC and 3D PL fractal properties with 2D BC properties are of potentially high importance and established in the present work. Finally, a comparison of these correlations with a previous one (not considering k) is performed, and comparison results show that the new correlations are more accurate.

Keywords: aggregation; agglomeration; fractal properties; box-counting prefactor; power law prefactor; structure in 3D; projections in 2D

Citation: Wang, R.; Singh, A.K.; Kolan, S.R.; Tsotsas, E. Investigation of the Relationship between the 2D and 3D Box-Counting Fractal Properties and Power Law Fractal Properties of Aggregates. *Fractal Fract.* **2022**, *6*, 728. https://doi.org/10.3390/fractalfract6120728

Academic Editors: Mikhail Avdeev and Oleksandr Tomchuk

Received: 14 November 2022
Accepted: 7 December 2022
Published: 9 December 2022

1. Introduction

Aggregates made of nano-sized spherical primary particles have complex and irregular structures. Aggregates of this kind occur in many practical applications, such as in colloidal, aerosol, or combustion systems [1–3]. The irregularity of the aggregates can influence their chemical and physical properties, by changing, for example, their surface area [4], light extinction efficiency [5], or aerodynamic behavior [6]. Since the aggregates can be considered as fractal-like structures [7], it is acceptable to quantify their irregularity by means of the fractal dimension D_f, as proposed by Mandelbrot [8]. In recent years, the fractal dimension has been investigated and used in order to characterize the morphology of particle systems and porous media [9–11], including building materials [12], as well as in the context of transport equations for fractal media [13]. Regarding the aggregates of primary particles, the box-counting (BC) [14] and the power law (PL) [15] methods are the most common methods used to calculate the fractal dimension.

Complementary to the fractal dimension is the prefactor k, as a second fractal property, which has though received much less attention than D_f. It is worth pointing out that for a given aggregate size, the spatial distribution of primary particles in aggregates is dependent on both the fractal dimension and the prefactor [16,17]. The constituent primary particles of aggregates become more concentrated in space with an increase in either of these two parameters. In the frame of a power law, the prefactor has an influence on how the aggregate mass is filling up the space, independently of its size, and on how the primary particles are packed [18]. The prefactor has been associated with the porosity and lacunarity of the aggregates [19]. The variation of the prefactor as a function of the fractal dimension and the packing density has been discussed in [16]. However, the power law method needs to collect data from many aggregates with distributed size to, then, provide mean fractal properties ($D_{f,\ PL}$ and k_{PL}) for the whole particle population [20]. In contrast, the box-counting method (BC) is a simple mathematical method that enables the determination of fractal dimensions on a single aggregate [21,22]. However, there are no studies with respect to the BC prefactor k_{BC}, which is not even defined and evaluated in many cases. Moreover, interrelations between BC fractal properties and PL fractal properties are missing.

Three-dimensional (3D) information about the aggregates can visually and comprehensively describe the morphological properties of aggregates. Tomography is widely applied to obtain 3D scanning of aggregates. The inner structure of aggregates can be directly accessed by optical coherence tomography or micro-computed tomography (μ-CT) [23]. Pashminehazar et al. [21] investigated the morphological properties of amorphous maltodextrin aggregates with highly porous and soft structures by X-ray μ-CT. The morphology and microstructure of diesel soot particulate matter were investigated by synchrotron soft X-ray tomography in [24]. Those authors calculated the fractal dimensions of agglomerates and diesel soot particulate matter by image analysis. However, when the aggregates are composed of nano-sized primary particles, their 3D data are difficult and expensive to obtain with the necessary resolution. It is, however, relatively easy and quick to get the 2D data of such aggregates by SEM or TEM. Light scattering and electron microscope methods for calculating the fractal dimension of fumed silica are compared in [25]. Quantitative analysis of the fractal dimension of soot aggregates by SEM and image processing techniques was performed by Chakrabarty et al. [26] to find the dependence of particle morphology on the electrical charging of particles. A new method was proposed in [27] to estimate the fractal dimension of individual soot aggregates, which can be applied to TEM images. Therefore, the development of a correlation between 2D and 3D fractal properties of aggregates would be highly beneficial, because then the 3D fractal properties of aggregates could be obtained from 2D fractal properties by means of the correlation. Wang et al. [28] proposed a 2D projection method to obtain the minimum overlapping between primary particles and built a correlation between 2D BC fractal dimension and the 3D power law fractal dimension. However, this correlation neglects the effect of the prefactor, considering the prefactor to be constant and equal to 1.

In this study, this limitation is removed. A particle-cluster tunable aggregation model is applied to generate a series of aggregates with various fractal properties (based on the power law and denoted by $D_{f,PL}$ and k_{PL}) and with various numbers of primary particles N_p. This is the modified polydisperse tunable sequential aggregation (MPTSA) model from [29]. Compared to cluster–cluster models, the particle–cluster tunable aggregation model can predict realistic fractal properties of aggregates accurately and quickly. Then, the projection method that has been introduced in [28] is applied to get 2D data of the generated aggregates. Further, the box-counting method is applied to obtain the respective fractal properties both in 2D (denoted by $D_{f,BC,2D}$, $k_{BC,2D}$) as well as in 3D ($D_{f,BC,3D}$ and $k_{BC,3D}$). Not only the fractal dimension, but also the fractal prefactor is evaluated in this frame. Finally, correlations between 3D BC fractal properties and 3D PL fractal properties with 2D box-counting fractal properties are established. Prospectively, such correlations can be used to reconstruct the spatial structure of aggregates based just on planar microscopy images.

2. Methods

2.1. Power Law (PL) Method

Using the power law method to estimate the fractal properties (fractal dimension $D_{f,PL}$ and prefactor k_{PL}) of the aggregates requires knowledge of several parameters, namely of the mean radius of primary particles (R_p), the radius of gyration (R_g), and the number of primary particles (N_p). The above parameters combine with the fractal properties to the power law relationship,

$$N_p = k_{PL} \left(\frac{R_g}{R_p} \right)^{D_{f,PL}}. \tag{1}$$

In Equation (1), gyration radius R_g is one of the basic parameters to describe an aggregate since it is influenced by the spatial distribution of mass around the mass center of the aggregate. Thus, R_g depends on both, the aggregate size and the mass distribution in it. The illustration of R_g of an aggregate is shown in Figure 1.

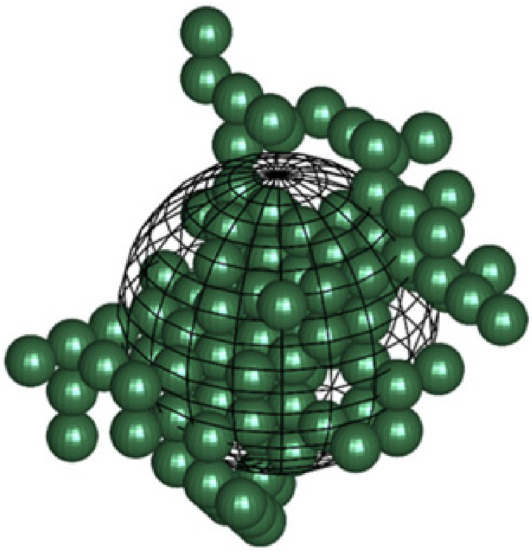

Figure 1. Illustration of the radius of gyration R_g of an aggregate.

In our present work, the constituent primary particles of aggregates are considered as monodisperse, so that R_g can be calculated according to [30] by means of the relationship

$$R_g = \sqrt{\frac{1}{2{N_p}^2} \sum_{i=0}^{N_p} \sum_{j=0}^{N_p} \left(R_i - R_j\right)^2}, \tag{2}$$

where R_i and R_j are the position vectors of the ith and the jth primary particles in the aggregate.

Equation (1) can be transformed into a logarithmic form:

$$\log \frac{R_g}{R_p} = D_{f,PL} \log N_p - k_{PL}. \tag{3}$$

According to Equation (3), plotting N_p versus R_g/R_p in logarithmic coordinates results in a linear regression that can be used to correlate $\log N_p$ and $\log(R_g/R_p)$. Then, the linear regression slope is fractal dimension $D_{f,\ PL}$ and the intercept is prefactor k_{PL}.

The power law method is an averaging method, which means that this method requires to collect data from a relatively large number of aggregates with distributed size and provides mean fractal properties ($D_{f,\ PL}$ and k_{PL}) of the whole particle population.

2.2. Box-Counting (BC) Method

The box-counting method is a relatively simple mathematical method that enables the determination of fractal properties on a single aggregate. This method can estimate the fractal dimension for aggregates with or without self-similarity. As discussed in Wang et al. [28], Strenzke et al. [31], and Pashminehazar et al. [21], the BC method can be used on both 2D and 3D aggregates.

The key point of the BC method is to create a grid with the same number of unit boxes (n) in each direction (for 3D, x, y and z directions, and one direction less for 2D). The number of boxes n varies with the scaling factor, ε, as shown in Figure 2. Typically, n has the value of a power of 2: it starts with 2 and ends with a limiting number (Sn). Sn is related to the resolution, for example, the number of voxels in 3D X-ray scans or the number of pixels of 2D microscopy images. The effect of Sn has been discussed in [28], Sn = 512 having been selected for this work. Then, the BC fractal dimension (denoted by $D_{f,\,BC}$) is estimated by the dynamic relationship between the number of boxes that are occupied by the aggregate $N(\varepsilon)$ and the scaling factor ε:

$$D_{f,\,BC} = \lim_{\varepsilon \to 0}\left(\frac{\log(N(\varepsilon))}{\log\left(\frac{1}{\varepsilon}\right)}\right). \tag{4}$$

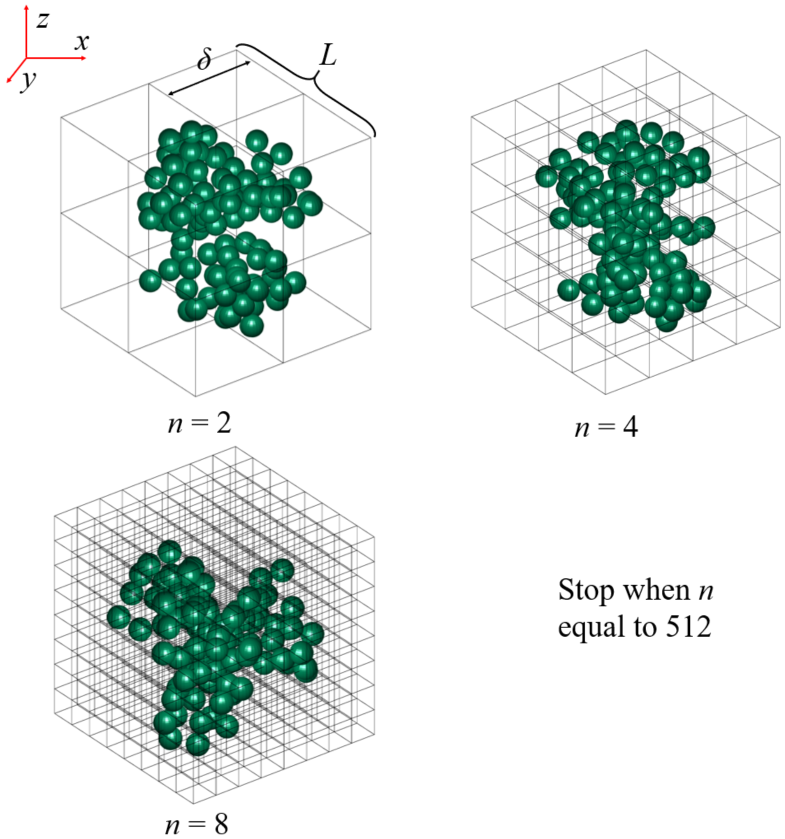

Figure 2. The evolution of n (=1/ε) in the 3D box-counting method.

In Figure 2, L is the side length of the whole grid and δ is the size of one box. The definition and determination of L have been investigated in [28], and in this work the same setting of L as in [28] has been applied when using the BC method. The relationship of L with respect to δ and ε is

$$L = n\delta = \frac{\delta}{\varepsilon}. \tag{5}$$

As shown in Figure 2, δ cannot reach zero. Thus, it is required to count the changing number $N(\varepsilon)$ of corresponding boxes with different side lengths, decreasing the value of ε for several times. Plotting $N(\varepsilon)$ versus $1/\varepsilon$ on a log-log plot gives a straight line with the least square method, and the absolute value of the slope of this line is the box-counting fractal dimension. Thus, $D_{f,\,BC}$ is calculated through the equation

$$y = D_{f,\,BC}\,x + k_{BC}. \tag{6}$$

where y represents $\log(N(\varepsilon))$, x is $\log(1/\varepsilon)$, and k_{BC} is the BC fractal prefactor. Comparing Equations (3) and (6), one can see that the slope of both equations represents the fractal dimension, whereas the intercept represents the prefactor. The relationship between BC fractal properties and PL fractal properties is discussed in Section 3.

2.3. Aggregate Generation

Here, a tunable aggregation model is applied to generate a series of aggregates with various fractal properties and different numbers of primary particles. This is the modified polydisperse tunable sequential aggregation model (MPTSA) from [29]. In this aggregate generation model, the input parameters are the fractal dimension $D_{f,\ PL}$, the prefactor k_{PL}, the number of primary particles N_P, and the radius of primary particles R_p. The flowchart of the MPTSA model is shown in Figure 3.

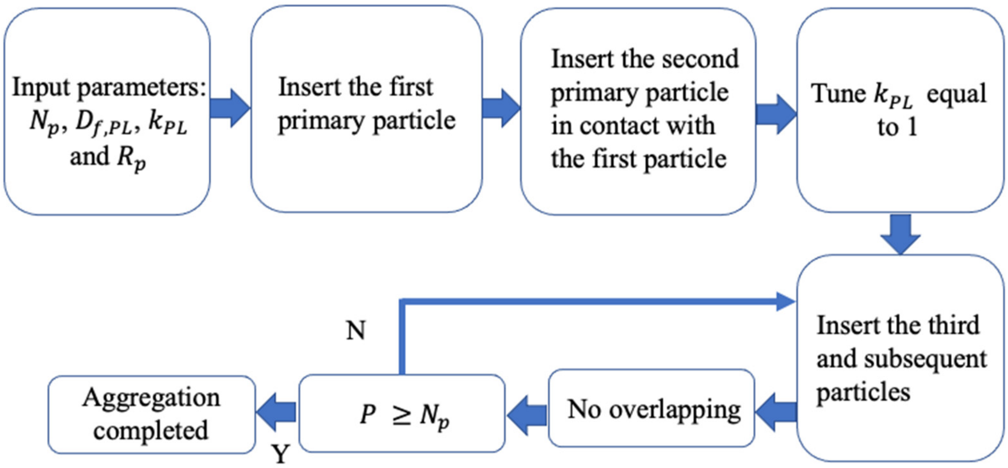

Figure 3. Flowchart of the MPTSA model.

The first primary particle is allotted to the center of the simulation space. Next, a point is selected on the surface of the first particle, and the second particle is placed adjacent to this point. As discussed in [32], there is a limitation of prefactor in the tunable sequential algorithm. So, the input fractal dimension $D_{f,\ PL}$ and prefactor k_{PL} are tuned to $D_{f,\ t}$ and k_t(=1) by the following equation [32],

$$D_{f,t} = D_{f,PL}\left(\frac{\log\left(\frac{N_p}{1}\right)}{\log\left(\frac{N_p}{k_{PL}}\right)}\right). \quad (7)$$

Then, the third and subsequent particles are inserted one by one. The center of each additional primary particle is located on a sphere of radius T

$$T^2 = \frac{P^2 {R_p}^2}{P-1}\left(\frac{P}{k_t}\right)^{\frac{2}{D_{f,t}}} - \frac{0.6P{R_p}^2}{N-1} - P{R_p}^2\left(\frac{P-1}{k_t}\right)^{\frac{2}{D_{f,t}}}. \quad (8)$$

Here, P ranges from 3 to N_p. The precise position on the sphere of radius T is chosen to have point contact with the new primary particle without overlapping. The addition of primary particles is continued one by one until $P \geq N_p$.

For illustration, we first generated a series of aggregates using the MPTSA model with different fractal properties ($D_{f,\ PL}$ and k_{PL}) and the same number of primary particles (N_p = 50), as shown in Figure 4. It can be seen from Figure 4 that both $D_{f,\ PL}$ and k_{PL} can affect the structural and morphological properties of aggregates. When $D_{f,\ PL}$ or k_{PL} increases gradually, the constituent primary particles tend to be more and more concentrated around the center point of the aggregate, which more and more resembles a sphere. However, the morphology of aggregates is more sensitive upon $D_{f,\ PL}$ than upon k_{PL}

(variation of $D_{f,\ PL}$ is from 1.8 to 3.0, whereas the variation of k_{PL} is from 1.0 to 7.0). This is due to the fact that k_{PL} is the prefactor, not the exponent of Equation (1).

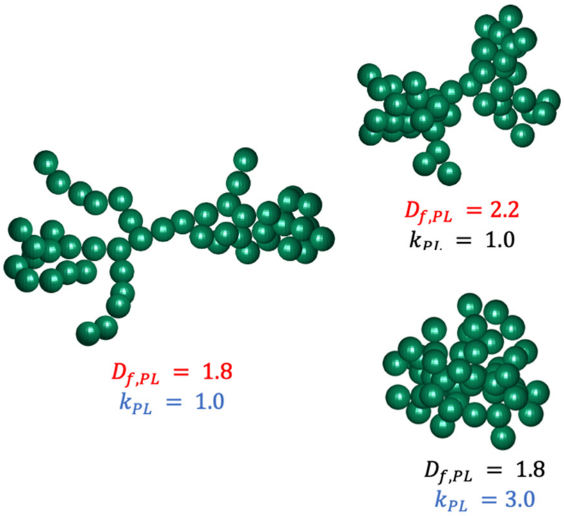

Figure 4. Morphological properties of aggregates with different $D_{f,\ PL}$ and k_{PL}.

3. Results and Discussion

3.1. Effective Range of Prefactor k_{PL}

The prefactor k_{PL} is an important parameter to describe the structural and morphological properties of aggregates, as shown in Figure 4. Therefore, and with values of $D_{f,\ PL}$ being in the range of 1 to 3, the question arises about the effective range that values of the prefactor k_{PL} may attain. For a first orientation, we summarized values of k_{PL} for aggregates with different $D_{f,PL}$ from the literature in Table 1.

Table 1. Values of k_{PL} and $D_{f,PL}$ from previous work.

References	k_{PL}	$D_{f,PL}$
Mountain and Mulholland [33]	5.80	1.90
Wu and Friedlander [18]	1.30	1.84
Puri et al. [34]	9.00	1.74
Sorensen and Roberts [16]	8.50	1.82
Ouf et al. [35]	2.44	1.78
Brasil et al. [36]	1.27	1.82

Table 1 shows a spread of k_{PL} from 1.27 to 9.0. However, the variation of $D_{f,PL}$ is small in the previous research, and derivations are not always detailed and clear. Therefore, we have decided to test the effective range of k_{PL} with the help of aggregates generated by the MPTSA model.

In the power law relationship (Equation (1)), the radius of gyration R_g can describe the spatial mass distribution around the mass center of the aggregate. As a criterion for the effective range of k_{PL}, we compare the radius of gyration calculated by Equation (1), denoted by $R_{g,PL}$, to the radius of gyration from generated aggregates according to Equation (2), denoted by $R_{g,MP}$. Both $R_{g,MP}$ and $R_{g,PL}$ are obtained with the same input parameters. The comparison is quantified by the ratio

$$Ra = \frac{R_{g,PL}}{R_{g,MP}}. \tag{9}$$

If Ra of the generated aggregate is greater than 99.99%, then k_{PL} is assumed to have been in its effective range.

Next, we generated in the frame of this evaluation two groups of aggregates with different fractal dimensions and prefactors. In the first group, the number of primary particles was N_p = 50, with $D_{f,PL}$ = 1.8:0.2:2.8 and k_{PL} varying from 0.9 to 5.0 in steps of 0.1. As for the second group, it had N_p = 300, $D_{f,PL}$ = 1.8:0.2:2.8, and k_{PL} = 0.9:0.1:10. The radius of primary particles R_p was constant and equal to 0.2 mm, but the absolute value of this variable has no influence on the results. The relationship of k_{PL} and $D_{f,PL}$ with Ra, based on two different values of N_p, is shown in Figure 5.

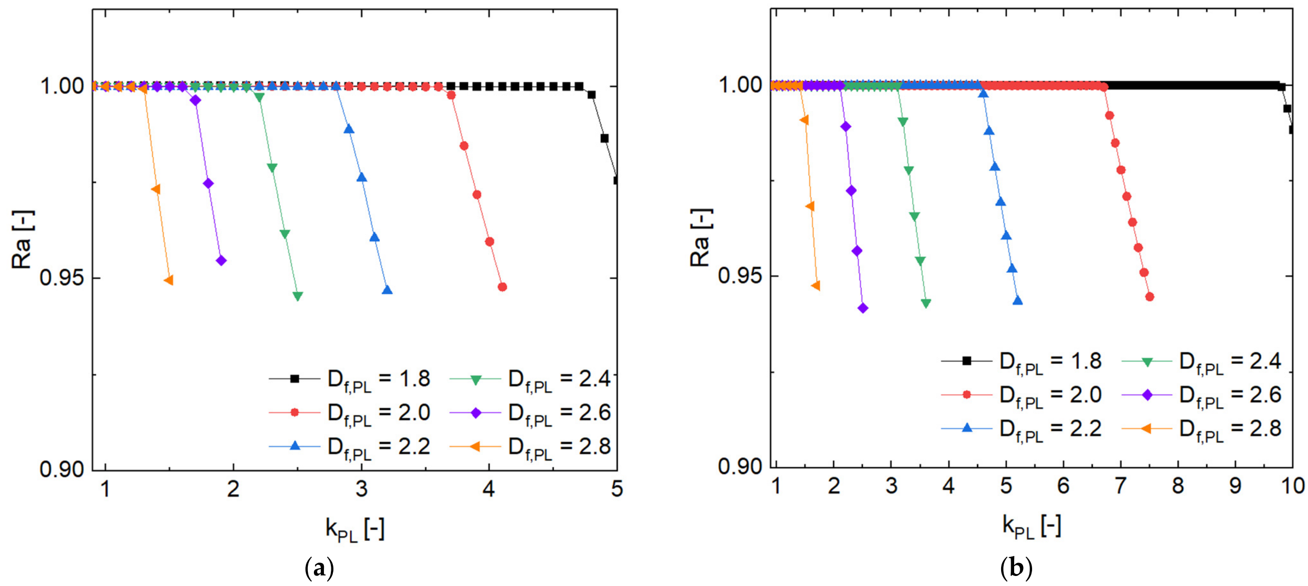

Figure 5. Influence of k_{PL} and $D_{f,PL}$ on Ra for different N_p, (**a**) N_p = 50, (**b**) N_p = 300.

As can be seen in Figure 5a,b, all the curves show the same trend: at the beginning, Ra of the aggregates does not change with increasing k_{PL}, being on a plateau with $Ra = 1$. Then, as k_{PL} increases, all curves show an inflection point, after which Ra decreases dramatically. When N_p is the same, the main difference among the curves is in the length of their plateau regions; aggregates with a smaller $D_{f,PL}$ show a longer plateau with $Ra = 1$ over k_{PL}. This means that the aggregates with smaller $D_{f,PL}$ have a broader effective range of k_{PL}. Besides, by comparing Figure 5a,b at the same $D_{f,PL}$, we can find that the effective range of k_{PL} of aggregates with smaller N_p(=50) is narrower than in the case of larger N_p(=300). The horizontal axis coordinates of the inflection points on each curve are considered as the upper limit of the effective range of k_{PL} under conditions specified by different $D_{f,PL}$ and N_p. Respective values are shown in Table 2.

Table 2. Lower and upper limits of the effective range of k_{PL} for different $D_{f,PL}$ and N_p.

$D_{f,PL}$	N_p = 100	N_p = 300
1.8	[0.9, 4.7]	[0.9, 9.7]
2.0	[0.8, 3.6]	[0.8, 6.9]
2.2	[0.7, 2.8]	[0.7, 4.5]
2.4	[0.6, 2.1]	[0.6, 3.1]
2.6	[0.5, 1.6]	[0.5, 2.1]
2.8	[0.4, 1.2]	[0.4, 1.4]

In Figure 5a, when k_{PL} is larger than 4.7 at N_p = 50 and $D_{f,PL}$ = 1.8, then the Ra of the aggregates is less than 1. This is since with an additional increase of k_{PL} (>4.7), the primary particles of these aggregates can no longer be concentrated further in space. So, $R_{g,MP}$ of these aggregates does not change with further increasing k_{PL}. For example, as shown in Figure 4, the structural and morphological characteristics of the aggregate with $D_{f,PL}$ = 1.8 and k_{PL} = 4.7 are the same as those of the aggregate with $D_{f,PL}$ = 1.8 and k_{PL} = 7.0, with $R_{g,MP}$ of these two aggregates being same and equal to 0.74 mm. However, $R_{g,PL}$ calculated formally from Equation (1) continues to decrease as k_{PL} increases, namely from $R_{g,PL}$ = 0.74 mm for aggregates with $D_{f,PL}$ = 1.8 and k_{PL} = 4.7, to $R_{g,PL}$ = 0.6 mm for aggregates with $D_{f,PL}$ = 1.8 and k_{PL} = 7.0. Therefore, when $D_{f,PL}$ = 1.8 and k_{PL} > 4.7, the ratio Ra of the aggregates is less than unity, meaning that k_{PL} has moved outside of its effective range.

As to the lower limit of k_{PL}, it has been determined by decreasing its value in steps of 0.1. This process stops when the MPTSA model ceases being able to generate the aggregate. Until then, the values of Ra of the generated aggregates remain equal to 1. The minimum k_{PL} at which aggregates can be generated is the lower limit of the effective range. Values for different $D_{f,PL}$ and N_p are shown in Table 2.

In addition to the above method that presupposes the generation of agglomerates by means of the MPTSA algorithm, a much simpler, algebraic estimation of the limits of the effective range of k_{PL} has also been implemented in the present work. According to Equation (1), k_{PL} shows a negative relationship to R_g/R_p under fixed N_p and $D_{f,PL}$,

$$k_{PL} = N_p/(R_g/R_p)^{D_{f,PL}}. \tag{10}$$

Therefore, when N_p and $D_{f,PL}$ are fixed and R_g/R_p minimal, k_{PL} takes its upper limit value. The lower limit of k_{PL} occurs when the situation is conversed (R_g/R_p at maximum value). The radius of gyration R_g of an aggregate shows the mass distribution around the aggregate center of mass. In our present work, the radius of primary particles R_p is constant at 0.2 mm. Therefore, when two aggregates with the same N_p show different R_g, the lower value of R_g indicates that the mass (primary particles) of the aggregate is more concentrated at the center of mass. So, the minimum R_g/R_p is reached when the morphology of the aggregate is like that of a sphere, which is here assumed to happen for an aggregate with $D_{f,PL}$ = 3.0 and k_{PL} = 1.0. On the contrary, the relative gyration radius R_g/R_p of the aggregates is maximum when the primary particles of the aggregates are most dispersed, assumed here to be the case for aggregates with $D_{f,PL}$ = 1.7 and k_{PL} = 1.0. Minimal R_g/R_p (at $D_{f,PL}$ = 3.0 and k_{PL} = 1.0) and maximal R_g/R_p (at $D_{f,PL}$ = 1.7 and k_{PL} = 1.0) of aggregates with different N_p are calculated by Equation (1), the results are summarized in Table 3.

Table 3. Minimal R_g/R_p ($D_{f,PL}$ = 3.0 and k_{PL} = 1.0) and maximal R_g/R_p ($D_{f,PL}$ = 1.7 and k_{PL} = 1.0) of aggregates with different N_p.

N_p	Minimal R_g/R_p	Maximal R_g/R_p
5	1.71	2.58
50	3.68	9.99
100	4.64	15.01
150	5.31	19.06
200	5.85	22.57
250	6.30	25.74
300	6.69	28.65

Then, minimal R_g/R_p and maximal R_g/R_p of the aggregates with different N_p are substituted into Equation (10), and upper and lower limits of the effective range are obtained for different $D_{f,PL}$, respectively. The lower and upper limits of the effective range of k_{PL} that have been estimated in this way are shown in Table 4.

Table 4. Upper limit and lower limit of effective range of k_{PL} from the simplified estimation without aggregate generation.

N_p	$D_{f,PL}$ = 1.8	$D_{f,PL}$ = 2.0	$D_{f,PL}$ = 2.2	$D_{f,PL}$ = 2.4	$D_{f,PL}$ = 2.6	$D_{f,PL}$ = 2.8
5	[0.91, 1.90]	[0.75, 1.71]	[0.62, 1.54]	[0.52, 1.38]	[0.43, 1.24]	[0.35, 1.11]
50	[0.79, 4.78]	[0.50, 3.68]	[0.32, 2.84]	[0.20, 2.19]	[0.13, 1.68]	[0.08, 1.30]
100	[0.76, 6.31]	[0.44, 4.64]	[0.26, 3.41]	[0.15, 2.51]	[0.09, 1.85]	[0.05, 1.36]
150	[0.74, 7.42]	[0.41, 5.31]	[0.23, 3.80]	[0.13, 2.72]	[0.07, 1.95]	[0.04, 1.40]
250	[0.73, 8.33]	[0.39, 5.85]	[0.21, 4.11]	[0.11, 2.89]	[0.06, 2.03]	[0.03, 1.42]
300	[0.72, 9.10]	[0.38, 6.30]	[0.20, 4.36]	[0.10, 3.02]	[0.05, 2.09]	[0.03, 1.44]

Comparing Tables 2 and 4, we can find that the upper limit of k_{PL} obtained by use of the MPTSA model is close (slightly smaller) to the results of the simplified estimation. The lower limit of k_{PL} in Table 2 is nearly equal to the lower limit value of k_{PL} for aggregates with the smallest N_p (= 5) in Table 4.

3.2. Relationship between BC Fractal Properties and PL Fractal Properties

In this section, we generated a series of aggregates with different fractal properties ($D_{f,PL}$ and k_{PL}) and N_p by the MPTSA model, with N_P varying from 100 to 300 in steps of 50 and $D_{f,PL}$ = 1.8:0.2:2.8. The investigated range of k_{PL} for each $D_{f,PL}$ is shown in Table 5. Those ranges correspond to the ranges for N_P = 100 from Table 4, being more restrictive in comparison to the ranges for aggregates with a larger number of primary particles. Consequently, all the generated aggregates are safely within the effective range of k_{PL} values. The primary particles of generated aggregates are monodispersed in the present work, with the radius of primary particles formally set at 0.2 mm. To capture stochastic variations, each aggregate is generated five times with the same input parameters.

Table 5. Realized ranges of k_{PL} for aggregates with different $D_{f,PL}$.

$D_{f,PL}$	Lower Limit k_{PL}	Upper Limit k_{PL}
1.8	0.9	6.3
2.0	0.8	4.6
2.2	0.7	3.4
2.4	0.6	2.5
2.6	0.5	1.8
2.8	0.4	1.3

In the further course of evaluation, a projection method proposed by [28] is applied to get 2D data for the generated aggregates. Then, both 3D and 2D box-counting methods are applied to estimate 3D BC fractal properties ($D_{f,BC,3D}$ and $k_{BC,3D}$) and 2D BC fractal properties ($D_{f,BC,2D}$ and $k_{BC,2D}$) of the generated aggregates. Next, aggregates generated with different N_p (=100, 200 and 300) and $D_{f,PL}$ (=1.8 and 2.8) are chosen to investigate the relationships between $D_{f,BC,3D}$ and $D_{f,BC,2D}$ with k_{PL}. The averages of $D_{f,BC,2D}$ and $D_{f,BC,3D}$ over the five realizations are shown in Figure 6 for the selected aggregates. Furthermore, averages ($D_{f,BC,2D}$ and $D_{f,BC,3D}$) over each entire aggregate series (with N_p = 100:50:300) are also plotted in Figure 6 against k_{PL}.

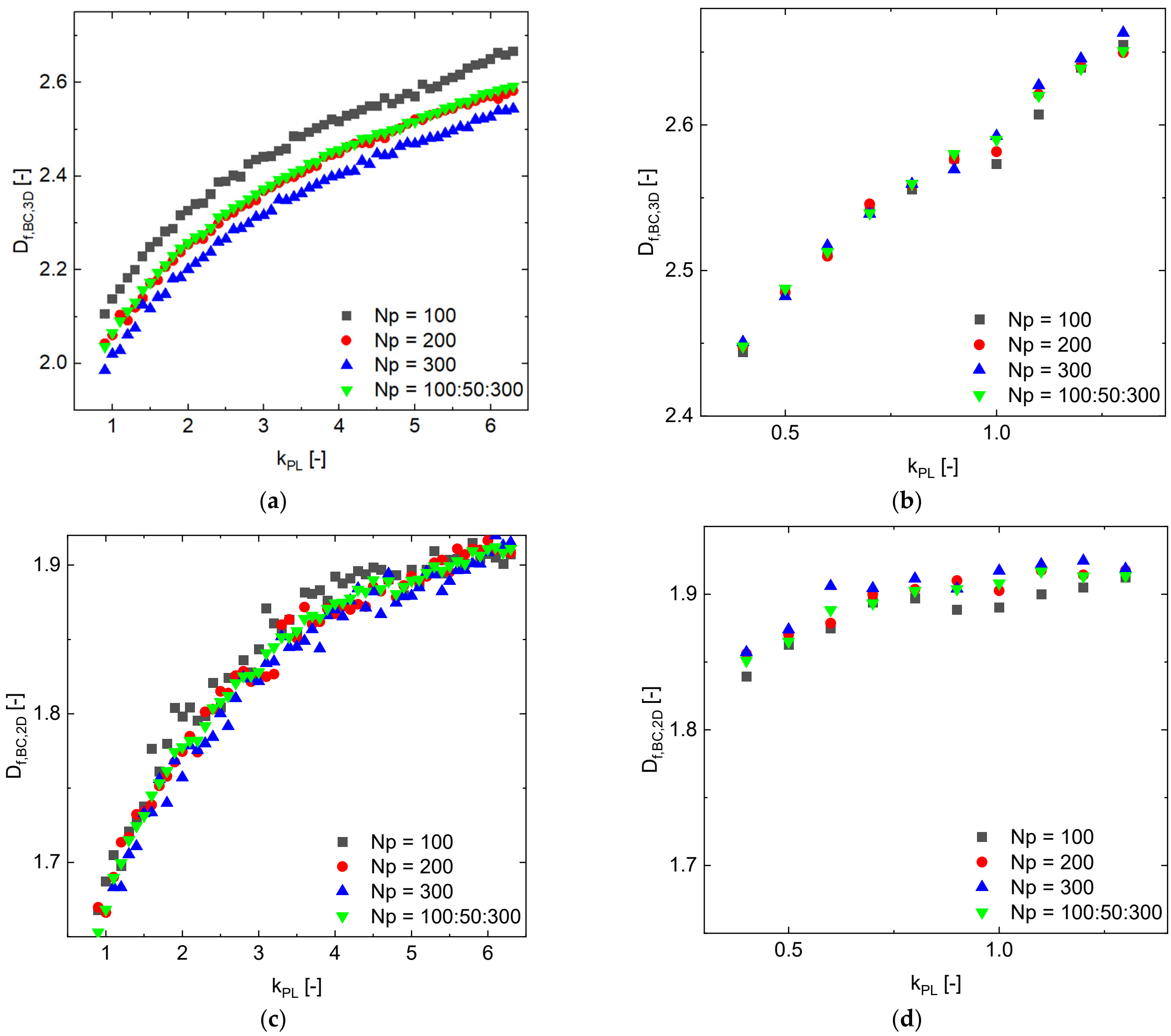

Figure 6. Relationship between $D_{f,BC,3D}$ and $D_{f,BC,2D}$ with k_{PL} : (**a**) $D_{f,PL}$ = 1.8 and BC in 3D, (**b**) $D_{f,PL}$ = 2.8 and BC in 3D, (**c**) $D_{f,PL}$ = 1.8 and BC in 2D, (**d**) $D_{f,PL}$ = 2.8 and BC in 2D.

All the curves in Figure 6 show the same trend, namely of BC fractal dimensions increasing with increasing k_{PL}. This is due to the fact that with the increase of k_{PL}, the distribution of primary particles becomes more and more concentrated (as shown in Figure 4). In the BC method, the number of boxes (N) occupied by aggregates is larger when the primary particles of aggregates are more concentrated [28]. According to Equation (4), N and BC fractal dimensions show a positive relationship. Therefore, the BC fractal dimension increases as k_{PL} increases.

Moreover, the trend in the variation of $D_{f,BC,2D}$ with k_{PL} in Figure 6d ($D_{f,PL}$ = 2.8 and BC in 2D) is slightly different from the other three figures (Figure 6a–c). In Figure 6d, $D_{f,BC,2D}$ initially increases with increasing k_{PL} (0.4 to 0.8), but then the value of $D_{f,BC,2D}$ starts fluctuating around 1.91 as k_{PL} further increases. This is because the calculation of the 2D BC fractal dimension of the aggregates is based on their projection. The purpose of projection method in this work is to get the least overlapping between primary particles (the maximum projected area of the aggregates) [28]. The morphology of the aggregates is though close to spherical when aggregates with a high fractal dimension and prefactor are considered [27] (i.e., $D_{f,PL}$ = 2.8 and k_{PL} > 0.8). Therefore, the 2D maximum projection area of these aggregates is almost constant with increasing k_{PL}, and the same holds for

$D_{f,BC,2D}$ values since these are directly affected by the projection area (positive relationship). Therefore, the $D_{f,BC,2D}$ value of the mentioned kind of aggregates floats around 1.91. In less obvious but analogous way, it can be seen from Figure 6c that the $D_{f,BC,2D}$ values of fluffy aggregates also float around 1.91 when the value of k_{PL} is large enough (> 5.5, in this case). In addition, the values of averages ($D_{f,BC,2D}$ and $D_{f,BC,3D}$) over the entire aggregate series (with N_p = 100:50:300) are generally close to the values for primary particle number in the middle of the series (N_p = 200).

3.3. Correlation between 3D BC Fractal Properties and 2D BC Fractal Properties

It is hard or even impossible to obtain the 3D fractal properties of aggregates composed of very small primary particles or nanoparticles by X-ray µ-CT, because of limitation in the spatial resolution of this imaging method. However, the 2D fractal properties of such aggregates can easily be retrieved by SEM or TEM. Therefore, a correlation between 2D and 3D fractal properties is necessary to be established. In this section, the correlation between 2D and 3D BC fractal properties is discussed first. Furthermore, the correlation between 2D BC and 3D PL fractal properties is discussed in the next section.

In Figure 7, the relationship between $k_{BC,2D}$ and $k_{BC,3D}$ for the aggregates with various $D_{f,PL}$ (=1.8:0.2:2.8) is shown. Values of $k_{BC,2D}$ and $k_{BC,3D}$ have been averaged over all N_p (from 100 to 300 in steps of 50) of the entire aggregate series and then over five realizations.

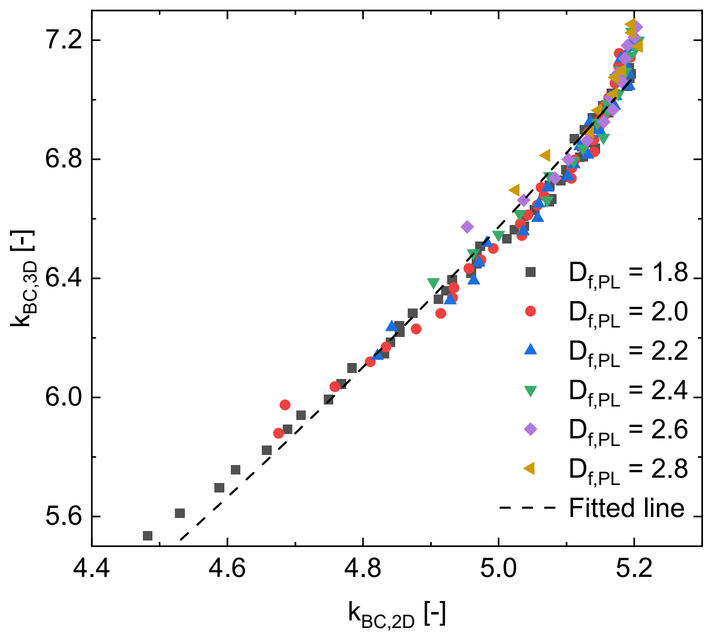

Figure 7. Relationship between $k_{BC,2D}$ and $k_{BC,3D}$ based on various $D_{f,PL}$.

As shown in Figure 7, $k_{f,BC,3D}$ increases with $k_{BC,2D}$ for any value of power law fractal dimension. All data points can, thus, be described by one and the same power regression,

$$k_{BC,3D} = 1.0262\mathrm{e}^{0.3714 k_{BC,2D}} \left(\mathrm{R}^2 = 0.9705\right). \tag{11}$$

The average values of $D_{f,BC,3D}$ (over five iterations) and $k_{BC,3D}$ for the aggregates with different $D_{f,PL}$ are plotted in Figure 8. From Figure 8 we can find that the value of $D_{f,BC,3D}$ is linearly increasing with $k_{BC,3D}$. The respective linear regression for all the aggregates is

$$D_{f,BC,3D} = 0.3585 k_{BC,3D} + 0.0423 \left(\mathrm{R}^2 = 0.9994\right). \tag{12}$$

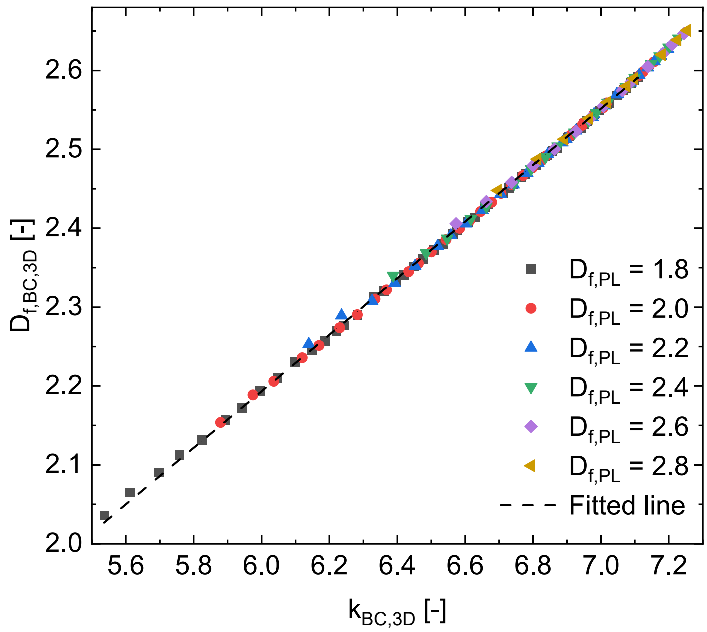

Figure 8. Correlation between $k_{BC,3D}$ and $D_{f,BC,3D}$ for aggregates with different $D_{f,PL}$.

A combination of Equations (11) and (12) can be used to obtain 3D BC fractal properties ($k_{BC,3D}$ and $D_{f,BC,3D}$) from a given 2D BC prefactor $k_{BC,2D}$ or, by additionally involving the later Equation (17), from a given 2D BC fractal dimension $D_{f,BC,2D}$.

3.4. Correlation between 2D BC Fractal Properties and PL Fractal Properties

The relationship between k_{PL} and $k_{BC,2D}$ for aggregates with various $D_{f,PL}$(=1.8:0.2:2.8) is shown in Figure 9. Values of $k_{BC,2D}$ have been averaged over all N_p (from 100 to 300 in steps of 50) of the entire aggregate series and then over five realizations.

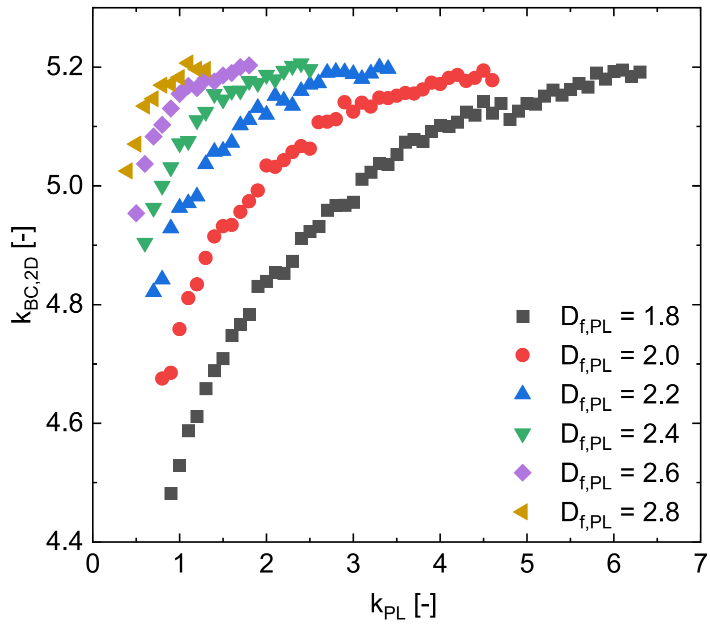

Figure 9. Relationship between k_{PL} and $k_{BC,2D}$ based on various $D_{f,PL}$(=1.8:0.2:2.8).

In Figure 9, $k_{BC,2D}$ is seen to increase with increasing k_{PL}; however, the growth rate of $k_{BC,2D}$ decreases as k_{PL} increases. As pointed out in Section 3.2, 2D BC fractal properties of aggregates are influenced by the 2D projection area [28], being positively interrelated. And when the morphology of the aggregates with higher k_{PL} or $D_{f,PL}$ has approached that of a sphere (as shown in Figure 4), the projection area of these aggregates changes only slightly with further increase in k_{PL}. Therefore, the rise of $k_{BC,2D}$ with k_{PL} flattens up at larger k_{PL} or $D_{f,PL}$. Here, an exponential function can be used for regression,

$$k_{BC,2D} = ae^{-bk_{PL}} + c. \tag{13}$$

In Equation (13), the curves with different $D_{f,PL}$ have different values of a, b, and c, as summarized in Table 6.

Table 6. Fitted values of a, b, and c corresponding to different $D_{f,PL}$.

$D_{f,PL}$	a	b	c
1.8	−1.182	0.551	5.223
2.0	−1.084	0.891	5.203
2.2	−0.928	1.244	5.210
2.4	−0.845	1.825	5.209
2.6	−0.805	3.311	5.197
2.8	−0.752	3.931	5.205

Then, correlations between, first, $D_{f,PL}$ and a, and second, between $D_{f,PL}$ and b are developed as follows:

$$a = 0.4389D_{f,PL} - 1.9419 \left(\mathrm{R}^2 = 0.9508\right), \tag{14}$$

$$b = 0.0363{D_{f,PL}}^{4.5778} \left(\mathrm{R}^2 = 0.9877\right). \tag{15}$$

The average value of c = 5.208 is used to represent this parameter.

Combining Equations (13)–(15), the correlation between $k_{BC,2D}$ and power law fractal properties is obtained:

$$k_{BC,2D} = \left(0.4389D_{f,PL} - 1.9419\right)e^{-0.0363{D_{f,PL}}^{4.5778}k_{PL}} + 5.208. \tag{16}$$

The averages of $D_{f,BC,2D}$ and $k_{BC,2D}$ over five realizations are plotted in Figure 10 for aggregates with different $D_{f,PL}$. As shown in Figure 10, $D_{f,BC,2D}$ increases linearly with $k_{BC,2D}$, according to the regression

$$D_{f,BC,2D} = 0.3693k_{BC,2D} - 0.0076 \left(\mathrm{R}^2 = 0.999\right). \tag{17}$$

Equations (16) and (17) are very important. Combining these two equations enables to predict power law fractal properties ($D_{f,PL}$ and k_{PL}) of aggregates from their 2D box-counting fractal properties ($k_{BC,2D}$ and $D_{f,BC,2D}$), the determination of which from microscope images is fast and easy in practice.

Therefore, the reliability of these two correlations is tested by a new series of aggregates generated by the MPTSA model. Here, three different values of $D_{f,PL}$ are used, namely $D_{f,PL}$ = 1.9, 2.3, and 2.7. The input number of primary particles N_p varied from 100 to 300 in steps of 50. The prefactor k_{PL} of the aggregates takes values from 0.9 to the upper limit of its effective range for each $D_{f,PL}$ (according to Table 5). The primary particles are still monodispersed, and the radius of primary particles is kept same as for the previously generated aggregates. Each aggregate with the same input parameters is generated five times. Then, the aggregates that have been generated in 3D are projected onto a 2D plane by the projection method from [28], and the 2D BC method is applied to estimate the 2D BC fractal properties for those projections. Then, the averages of $D_{f,BC,2D}$ and $k_{BC,2D}$ for each aggregate are calculated over five realizations. Substituting $k_{BC,2D}$ and $D_{f,BC,2D}$ into Equations (16) and (17), values of power law fractal properties (k_{PL} and $D_{f,PL}$) are finally calculated. Examples of calculated results for aggregates with $D_{f,PL}$ = 1.9 are summarized in Table 7.

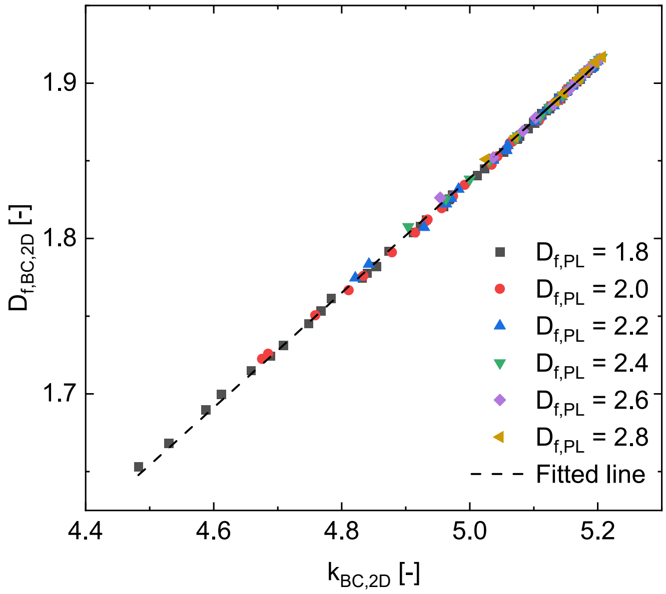

Figure 10. Correlation between $k_{BC,2D}$ and $D_{f,BC,2D}$ for aggregates with different $D_{f,PL}$.

Table 7. Predicted $D_{f,PL}$ and k_{PL} of aggregates with input $D_{f,PL}$ = 1.9.

Input k_{PL}	Calculated $D_{f,PL}$	Calculated k_{PL}
1.0	1.97	0.79
1.5	2.08	0.97
2.0	1.61	4.06
2.5	2.27	1.02
3.0	2.20	1.46

In Table 7, there is a notable difference between the input fractal parameters and the calculated values. This is due to the difficult inversion of Equations (16) and (17) for given $k_{BC,2D}$ and $D_{f,BC,2D}$. This is done by numerical optimization, which is though confronted with several flat and similar optima.

Whereas further improvement is desirable at this point, the ratio R_g/R_p, which is an important parameter for the morphological analysis of aggregates, can be applied to test the predicted values from Equations (16) and (17). It is recalled that Wang et al. [28] have recently established an original correlation between 2D BC fractal dimension and PL fractal dimension. This correlation, however, neglected the influence of k_{PL} and kept this parameter constant (=1). The correlation is

$$D_{f,PL} = 0.2015 D_{f,BC,2D}^{4.079}. \quad (18)$$

Predicted results ($D_{f,PL}$ and k_{PL}) from Equations (16) and (17) are substituted to Equation (1) to calculate R_g/R_p of the new series of aggregates ($D_{f,PL}$ = 1.9, 2.3, and 2.7, N_p = 100, 200, and 300). For the sake of comparison, $D_{f,BC,2D}$ of the new generated aggregates are substituted to Equation (18) to estimate their $D_{f,PL}$. Then, keeping k_{PL} as constant and equal to 1, another R_g/R_p is estimated by means of $D_{f,PL}$ predicted from Equation (18). Finally, the two kinds of R_g/R_p are compared in Figure 11 based on three N_p (= 100, 200, and 300). R_g/R_p calculated from prediction results of the equations in this research (Equations (16) and (17)) are denoted by "present", R_g/R_p calculated from the correlation of the previous work (Equation (18)) are denoted by "previous". In addition, the standard R_g/R_p which is calculated from the input parameters ($D_{f,PL}$, k_{PL}, and N_p) of the MPTSA model is also shown in Figure 11 (dotted lines). The R-square analysis represents the deviation of the predicted R_g/R_p (present or previous) to standard R_g/R_p.

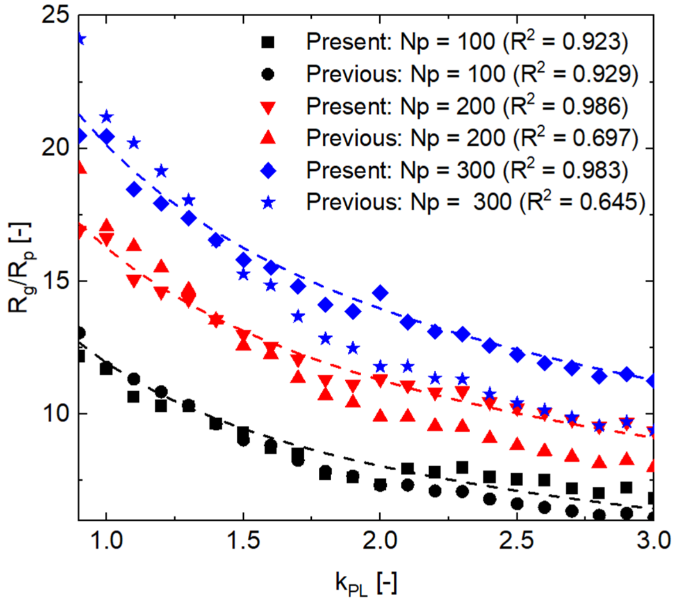

(**a**)

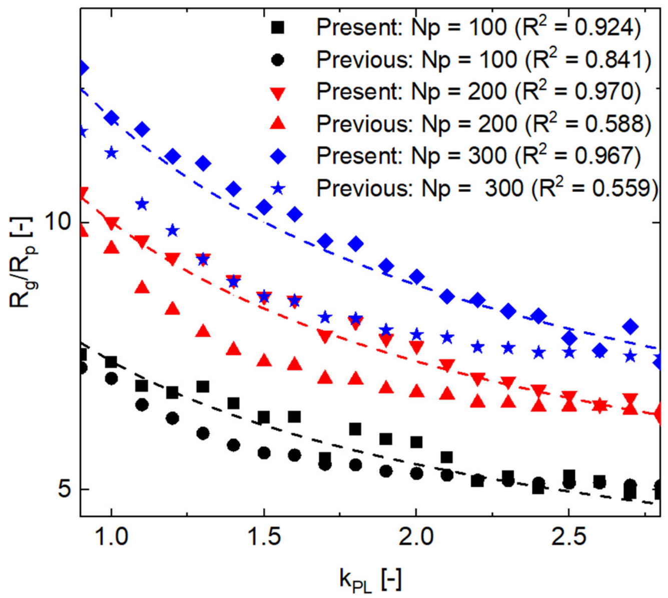

(**b**)

Figure 11. *Cont.*

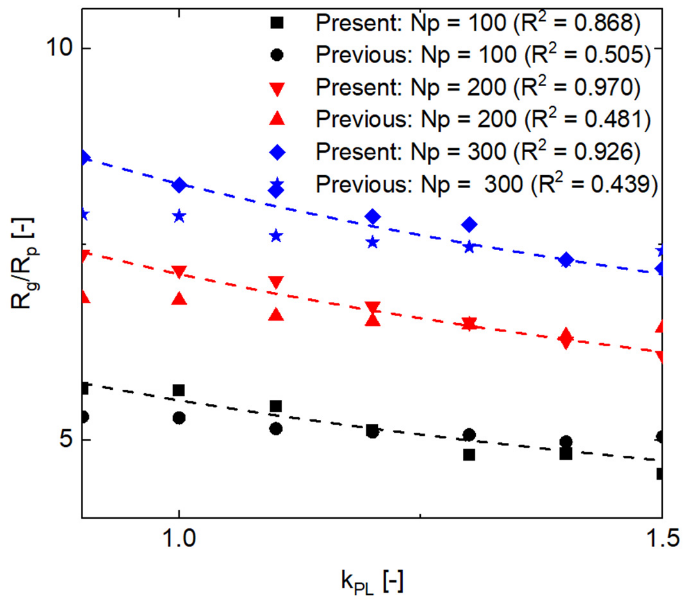

(**c**)

Figure 11. Comparison of two prediction methods by R_g/R_p: (**a**) $D_{f,PL}$ = 1.9, (**b**) $D_{f,PL}$ = 2.3, (**c**) $D_{f,PL}$ = 2.7.

As shown in Figure 11, when both $D_{f,PL}$ and N_p are small ($D_{f,PL}$ = 1.9 and N_p = 100), the difference between present predicted results (Equations (16) and (17)) and previous predicted results (Equation (18)) is insignificant, the R^2 of the two sets of results to the standard (input, reference) data being 0.923 and 0.929, respectively. However, when $D_{f,PL}$ or N_p increases, the R^2 of previous results decreases significantly. Especially when the aggregates with $D_{f,PL}$ = 2.7 and N_p = 300 are considered, the R^2 of previous results reaches a very low value of 0.439. However, the changes in $D_{f,PL}$ or N_p hardly affect the accuracy of the present results, which are based on predictions from Equations (16) and (17). In Figure 11, the minimum R^2 of present results is equal to 0.868 when $D_{f,PL}$ = 2.7 and N_p = 100.

4. Conclusions

This study aimed to investigate the fractal properties of aggregates made of primary particles. To enable this investigation, synthetic aggregates have been generated by an appropriate numerical method (MPTSA model) with various input parameters. Special emphasis was set on the variation of power law prefactor k_{PL}. Not every value of this parameter is reasonable, so that its so-called effective range had to be first determined. Therefore, we introduced a ratio Ra between two differently derived radii of gyration R_g as a criterion that can be used to judge whether aggregates are within the effective range of k_{PL} or not. Where $R_{g,MP}$ is estimated from generated aggregates (aggregates produced with the help of the MPTSA model) and $R_{g,PL}$ is obtained from the power law. Conceivable deviation of Ra from unity means out-of-range values of k_{PL}. A simplified method that works without aggregate generation is also proposed as an alternative to this rigorous approach.

In the main part of the work, a series of aggregates (with different fractal properties $D_{f,PL}$ and k_{PL}, and also with different number of primary particles N_p) is generated by the MPTSA model. Values of k_{PL} are taken from their effective ranges based on different N_p and power law fractal dimension $D_{f,PL}$. Next, a projection method proposed by [28] is applied to retrieve 2D information for the generated aggregates. Both the 3D BC fractal properties ($D_{f,BC,3D}$ and $k_{BC,3D}$) and the 2D BC fractal properties ($D_{f,BC,2D}$ and $k_{BC,2D}$) of the generated aggregates are calculated by the box-counting (BC) method.

Considering that the 3D fractal properties of aggregates composed of very small particles are hard to gain by means of X-ray μ-CT, or with the help of other tomographic methods, due to limited physical resolution, tractable pathways for their determination from more easily accessible information would be of great importance. Such information could be the 2D fractal properties of those aggregates, because 2D fractal properties can easily be extracted from SEM or TEM images. To this purpose, novel correlations between 3D BC fractal properties and 3D PL fractal properties with 2D BC fractal properties have been established with the help of synthetic aggregates. In addition, one more series of synthetic aggregates has been generated to validate the correlation between 2D BC and 3D PL fractal properties. The validation results are compared with the results of a previous correlation (not considering the variability of k_{PL}) as well as with results from the used input data as a benchmark. Present and previous results meet similarly well the benchmark only when both $D_{f,PL}$ and N_p are small ($D_{f,PL}$ = 1.9 and N_p = 100). However, our new correlations are more accurate for aggregates with higher $D_{f,PL}$ or N_p.

The generated aggregates in this work had monodispersed primary particles. Therefore, aggregates with polydisperse primary particles need to be also investigated, which is planned for near future.

Author Contributions: Conceptualization, R.W.; Methodology, R.W., A.K.S., S.R.K. and E.T.; Software, R.W.; Validation, R.W. and A.K.S.; Formal analysis, R.W.; Investigation, R.W.; Writing—original draft, R.W.; Writing—review & editing, E.T. All authors have read and agreed to the published version of the manuscript.

Funding: This research was funded by Deutsche Forschungsgemeinschaft (German Research Foundation) grant number 462225760.

Acknowledgments: The authors gratefully acknowledge the CSC (R.W.) and the BMBF (A.K.S., project 03INT609AA, COAGG) on the financial support for this research.

Conflicts of Interest: The authors declare no conflict of interest.

Nomenclature

D_f	fractal dimension, -
k	prefactor, -
L	side length of domain, m
n	number of unit boxes, -
N	number of boxes occupied by the object, -
N_p	number of primary particles, -
P	intermediate particle number, -
R_g	radius of gyration, m
R_P	mean radius of primary particles, m
Sn	limiting number of boxes, m
Greek letters	
δ	size of box, m
ε	scaling factor, -
Abbreviations	
BC	box-counting
MPTSA	modified polydisperse tunable sequential aggregation
PL	power law
SEM	scanning electron microscopy
TEM	transmission electron microscopy

References

1. Davis, J.; Molnar, E.; Novosselov, I. Nanostructure transition of young soot aggregates to mature soot aggregates in diluted diffusion flames. *Carbon* **2020**, *159*, 255–265. [CrossRef] [PubMed]
2. Kelesidis, G.A.; Goudeli, E.; Pratsinis, S.E. Flame synthesis of functional nanostructured materials and devices: Surface growth and aggregation. *Proc. Combust. Inst.* **2017**, *36*, 29–50. [CrossRef]

3. Wu, Y.; Cheng, T.; Liu, D.; Allan, J.D.; Zheng, L.; Chen, H. Light absorption enhancement of black carbon aerosol constrained by particle morphology. *Environ. Sci. Technol.* **2018**, *52*, 6912–6919. [CrossRef] [PubMed]
4. Dorigato, A.; D'amato, M.; Pegoretti, A. Thermo-mechanical properties of high density polyethylene–fumed silica nanocomposites: Effect of filler surface area and treatment. *J. Polym. Res.* **2012**, *19*, 9889. [CrossRef]
5. Liou, K.N.; Takano, Y.; Yang, P. Light absorption and scattering by aggregates: Application to black carbon and snow grains. *J. Quant. Spectrosc. Radiat. Transfer.* **2011**, *112*, 1581–1594. [CrossRef]
6. Baldelli, A.; Rogak, S.N. Morphology and Raman spectra of aerodynamically classified soot samples. *Atmos. Meas. Tech.* **2019**, *12*, 4339–4346. [CrossRef]
7. Bonczyk, P.A.; Hall, R.J. Fractal properties of soot agglomerates. *Langmuir* **1991**, *7*, 1274–1280. [CrossRef]
8. Mandelbrot, B.B. *The Fractal Geometry of Nature*; WH Freeman: New York, NY, USA, 1983; p. 406.
9. Xiao, B.; Li, Y.; Long, G. A fractal model of power-law fluid through charged fibrous porous media by using the fractional-derivative theory. *Fractals* **2022**, *30*, 2250072-446. [CrossRef]
10. Xiu, H.; Ma, F.; Zhao, X.; Liu, L.; Feng, P.; Ji, Y. Using fractal dimension and shape factors to characterize the microcrystalline cellulose (MCC) particle morphology and powder flowability. *Powder Technol.* **2020**, *364*, 241–250. [CrossRef]
11. Liang, M.; Fu, C.; Xiao, B.; Luo, L.; Wang, Z. A fractal study for the effective electrolyte diffusion through charged porous media. *Int. J. Heat Mass Transf.* **2019**, *137*, 365–371. [CrossRef]
12. Lü, Q.; Qiu, Q.; Zheng, J.; Wang, J.; Zeng, Q. Fractal dimension of concrete incorporating silica fume and its correlations to pore structure, strength and permeability. *Constr. Build. Mater.* **2019**, *228*, 116986. [CrossRef]
13. Wang, K. Exact traveling wave solutions for the local fractional Kadomtsov–Petviashvili–Benjamin–Bona–Mahony model by variational perspective. *Fractals* **2022**, *30*, 2250101. [CrossRef]
14. Feller, W. On boundaries and lateral conditions for the Kolmogorov differential equations. *Ann. Math.* **1957**, *65*, 527–570. [CrossRef]
15. Forrest, S.R.; Witten, J.; Thomas, A. Long-range correlations in smoke-particle aggregates. *J. Phys. A Math. Gen.* **1979**, *12*, L109. [CrossRef]
16. Sorensen, C.M.; Roberts, G.C. The prefactor of fractal aggregates. *J. Colloid Interface Sci.* **1997**, *186*, 447–452. [CrossRef] [PubMed]
17. Lapuerta, M.; Martos, F.J.; Martín-González, G. Geometrical determination of the lacunarity of agglomerates with integer fractal dimension. *J. Colloid Interface Sci.* **2010**, *346*, 23–31. [CrossRef]
18. Wu, M.K.; Friedlander, S.K. Note on the power law equation for fractal-like aerosol agglomerates. *J. Colloid Interface Sci.* **1993**, *159*, 246–248. [CrossRef]
19. Hu, B.; Koylu, U. Size and morphology of soot particulates sampled from a turbulent nonprefixed acetylene flame. *Aerosol. Sci. Technol.* **2004**, *38*, 1009–1018. [CrossRef]
20. Fabre, A.; Steur, T.; Bouwman, W.G.; Kreutzer, M.T.; van Ommen, J.R. Characterization of the stratified morphology of nanoparticle agglomerates. *J. Phys. Chem. C* **2016**, *120*, 20446–20453. [CrossRef]
21. Pashminehazar, R.; Kharaghani, A.; Tsotsas, E. Determination of fractal dimension and prefactor of agglomerates with irregular structure. *Powder Technol.* **2019**, *343*, 765–774. [CrossRef]
22. Zhang, L.; Dang, F.; Ding, W.; Zhu, L. Quantitative study of meso-damage process on concrete by CT technology and improved differential box counting method. *Measurement* **2020**, *60*, 107832. [CrossRef]
23. Pyrz, R. Application of X-ray microtomography to the study of polymer composites. *SAE Trans.* **1999**, *108*, 1312–1316. Available online: https://www.jstor.org/stable/44729518 (accessed on 10 May 2022).
24. Yan, F.; Song, J.; Zhuang, Y.; Qiu, L.; Meng, Z. Three-dimension soft X-ray tomographic reconstruction of particulates emitted from a diesel engine. *J. Aerosol. Sci.* **2021**, *156*, 105784. [CrossRef]
25. Ibaseta, N.; Biscans, B. Fractal dimension of fumed silica: Comparison of light scattering and electron microscope methods. *Powder Technol.* **2010**, *203*, 206–210. [CrossRef]
26. Chakrabarty, R.K.; Moosmüller, H.; Garro, M.A.; Arnott, W.P.; Slowik, J.G.; Cross, E.S.; Worsnop, D.R. Morphology based particle segregation by electrostatic charge. *J. Aerosol. Sci.* **2008**, *39*, 785–792. [CrossRef]
27. Lapuerta, M.; Ballesteros, R.; Martos, F.J. A method to determine the fractal dimension of diesel soot agglomerates. *J. Colloid Interface Sci.* **2006**, *303*, 149–158. [CrossRef]
28. Wang, R.; Singh, A.K.; Kolan, S.R.; Tsotsas, E. Fractal analysis of aggregates: Correlation between the 2D and 3D box-counting fractal dimension and power law fractal dimension. *Chaos Solitons Fractals* **2022**, *160*, 112246. [CrossRef]
29. Singh, A.K.; Tsotsas, E. A Fast and Improved Tunable Aggregation Model for Stochastic Simulation of Spray Fluidized Bed Agglomeration. *Energies* **2021**, *14*, 7221. [CrossRef]
30. Teraoka, I. *An Introduction to Physical Properties*; John Wiley & Sons, Inc.: New York, NY, USA, 2002; ISBN 978-0-471-38929-3.
31. Strenzke, G.; Janocha, M.; Bück, A.; Tsotsas, E. Morphological descriptors of agglomerates produced in continuously operated spray fluidized beds. *Powder Technol.* **2022**, *397*, 117111. [CrossRef]
32. Singh, A.K.; Tsotsas, E. A tunable aggregation model incorporated in Monte Carlo simulations of spray fluidized bed agglomeration. *Powder Technol.* **2020**, *364*, 417–428. [CrossRef]
33. Mountain, R.D.; Mulholland, G.W. Light scattering from simulated smoke agglomerates. *Langmuir* **1988**, *4*, 1321–1326. [CrossRef]

34. Puri, R.; Richardson, T.F.; Santoro, R.J.; Dobbins, R.A. Aerosol dynamic processes of soot aggregates in a laminar ethene diffusion flame. *Combust. Flame* **1993**, *92*, 320–333. [CrossRef]
35. Ouf, F.X.; Vendel, J.; Coppalle, A.; Weill, M.; Yon, J. Characterization of soot particles in the plumes of over-ventilated diffusion flames. *Combust. Sci. Technol.* **2008**, *180*, 674–698. [CrossRef]
36. Brasil, A.M.; Farias, T.L.; Carvalho, M.G. Evaluation of the Fractal Properties of Cluster? Cluster Aggregates. *Aerosol. Sci. Technol.* **2000**, *33*, 440–454. [CrossRef]